

Signatures of minor mergers in the Milky Way disc I: The SEGUE stellar sample

Facundo A. Gómez^{1,2*}, Ivan Minchev³, Brian W. O’Shea^{1,2,4},
 Young Sun Lee^{1,5}, Timothy C. Beers^{1,6}, Deokkeun An⁷, James S. Bullock⁸,
 Chris W. Purcell^{8,9}, Álvaro Villalobos¹⁰

¹ Department of Physics and Astronomy, Michigan State University, East Lansing, MI 48824, USA

² Institute for Cyber-Enabled Research, Michigan State University, East Lansing, MI 48824, USA

³ Leibniz-Institut für Astrophysik Potsdam (AIP), An der Sternwarte 16, D-14482, Potsdam, Germany

⁴ Lyman Briggs College, Michigan State University, East Lansing, MI 48825, USA

⁵ Joint Institute for Nuclear Astrophysics (JINA), Michigan State University, East Lansing, MI 48824, USA

⁶ National Optical Astronomy Observatory, Tucson, AZ 85719, USA

⁷ Department of Science Education, Ewha Womans University, Seoul 120-750, Republic of Korea

⁸ Center for Cosmology, Department of Physics and Astronomy, The University of California, Irvine

⁹ Department of Physics and Astronomy, The University of Pittsburgh

¹⁰ INAF-Osservatorio Astronomico di Trieste, Via Tiepolo 11, I-34143 Trieste, Italy

ABSTRACT

It is now known that minor mergers are capable of creating structure in the phase-space distribution of their host galaxy’s disc. In order to search for such imprints in the Milky Way, we analyse the SEGUE F/G-dwarf and the Schuster et al. (2006) stellar samples. We find similar features in these two completely independent stellar samples, consistent with the predictions of a Milky Way minor-merger event. We next apply the same analyses to high-resolution, idealised N-body simulations of the interaction between the Sagittarius dwarf galaxy and the Milky Way. The energy distributions of stellar particle samples in small spatial regions in the host disc reveal strong variations of structure with position. We find good matches to the observations for models with a mass of Sagittarius’ dark matter halo progenitor $\lesssim 10^{11} M_{\odot}$. Thus, we show that this kind of analysis could be used to provide unprecedentedly tight constraints on Sagittarius’ orbital parameters, as well as place a lower limit on its mass.

Key words: Galaxy: disc, structure – galaxies: formation – galaxies: kinematics and dynamics – methods: analytical – methods: N-body simulations

1 INTRODUCTION

It is now widely accepted that the gravitational pull exerted by a merging satellite galaxy can generate structure in the stellar disc of its more-massive host. A striking example of the outcome of these kind of interactions is the system composed of M51 and its companion galaxy, NGC 5195 (e.g. Oh et al. 2008; Dobbs et al. 2010). Previous studies have shown that prominent spiral structure is more commonly observed in galaxies located within groups or with companions (Kormendy & Norman 1979; Elmegreen & Elmegreen 1982, 1983). These observations highlighted the importance of tidal interactions on the struc-

ture of galactic discs. Although grand design spirals, such as the ones observed in M51, are related to massive companions (in this case, $M_{M51}/M_{NGC\ 5195} \gtrsim 0.3$), several theoretical studies have shown that much less massive satellites can also create phase-space structure in galactic discs (Quinn, Hernquist & Fullagar 1993; Tutukov & Fedorova 2006; Kazantzidis et al. 2008; Villalobos & Helmi 2008; Younger et al. 2008; Quillen et al. 2009; Minchev et al. 2009; Bird, Kazantzidis & Weinberg 2011; Gómez et al. 2012). Morphological features, such as spiral arms, warps, flares, central bars, and low surface brightness ringlike structures in the outskirts of a disc can be the result of either recent or ongoing accretion events.

Most of the previously-mentioned morphological features have been observed in the disc of our

* Email:fgomez@pa.msu.edu

own Galaxy (Levine et al. 2006; Momany et al. 2006; Cabrera-Lavers et al. 2007; Pohl et al. 2008; Newberg et al. 2002; Yanny et al. 2003), and various formation scenarios have been explored for most of them. An interesting example is the Monoceros ring, which is a low-latitude stellar structure spanning about 180° in Galactic longitude at nearly constant Galactocentric distance. It has been proposed that this structure could be the remnant of a tidally-disrupted satellite galaxy (Helmi et al. 2003; Ibata et al. 2003; Conn et al. 2005; Peñarrubia et al. 2005). More recently, several authors have argued that this dynamically cold ring could be the result of a tidal perturbation from a satellite galaxy on the Galactic disc (Kazantzidis et al. 2008; Younger et al. 2008; Quillen et al. 2009). In particular, the Sagittarius dwarf galaxy (Sgr) has been proposed as a possible perturber of the Milky Way, causing the emergence of the Monoceros ring as the far extension of a Galactic spiral arm (Purcell et al. 2011) and also potentially as a gravitational influence that circularised the orbit of a putative dwarf galaxy that could have been torn apart to become that same ring (Michel-Dansac et al. 2011). Motivated by recent studies on cosmological abundance matching (Conroy & Wechsler 2009; Behroozi, Conroy & Wechsler 2010), Purcell et al. (2011, hereafter P11) considered models of Sagittarius with total masses as large as $\sim 10\%$ of the Milky Way’s mass. These models can successfully reproduce not only dynamically cold structures such as the Monoceros ring, but also other global morphological features observed in the Milky Way. However, its impact on the phase-space structure of the Solar neighbourhood has not yet been explored.

As first shown by Minchev et al. (2009), the energy kick imparted by the gravitational potential of a satellite as it crosses the plane of the disc can strongly perturb the velocity field of disc stars located in local volumes such as the Solar neighbourhood. In stellar samples close to the Sun (i.e. distances ≤ 0.2 kpc), these perturbations can be observed in the u - v plane as arc-like features traveling in the direction of positive v , where u and v are the radial and tangential velocity components, respectively. In a follow-up study, Gómez et al. (2012) showed that the space defined by the energy and angular momentum of stars is a better choice than velocity space, as substructure remains visible even in much larger local volumes. Furthermore, they also showed that satellites with masses as small as 10% of the mass of the host can leave imprints in the phase-space distribution of Solar neighbourhood-like volumes that could be identified as late as ≈ 5 Gyr after the first satellite’s pericentre passage. Substructure associated with this mechanism, known as “ringing,” is expected to be better defined in the Galactic thick disc. This is because these stars spend relatively little time near the Galactic plane, where perturbations from the Galactic bar, spiral structure, and giant molecular clouds are more vigorous. Moreover, the thick disc is composed of a very old population of stars, with ages around 10 to 12 Gyr (Schuster et al. 2006; Bensby et al. 2007). Thus, most of its stars must have been in place at the time the hypothetical merger occurred.

An obvious question arises from our previous discussion: Could a satellite galaxy like Sagittarius have left imprints of its tidal interaction with the Milky Way’s thick disc in the

local stellar phase-space distribution? Previous attempts to describe features in the velocity field of the Solar neighbourhood have been primarily concerned with the dynamical effects induced by non-axisymmetric disc components, such as a central bar or self-gravitating spiral arms (see, e.g., Dehnen 2000; Fux 2001; Minchev et al. 2007; Minchev & Quillen 2008; Antoja et al. 2009; Minchev et al. 2010; Antoja et al. 2011; Quillen et al. 2011). These studies have focused their attention on very small local volumes, dominated mostly by populations of thin-disc stars. However, little attention has been paid to the identification and characterisation of substructure in local volumes of the Milky Way’s thick disc that may have originated as a response of the tidal interaction with a satellite galaxy (see, e.g., Minchev et al. 2009).

In this work we attempt to fill this gap by analysing a full 6D phase-space catalog of F/G-type dwarf stars from the Sloan Extension for Galactic Understanding and Exploration (SEGUE; Yanny et al. 2009). The great advantage of this catalog, as presented by Lee et al. (2011b, hereafter L11), is that it contains accurate estimates of $[\alpha/\text{Fe}]$ and $[\text{Fe}/\text{H}]$ ratios for a large fraction of its stars. This enables a chemical separation of the disc system into likely thin- and thick-disc populations, avoiding unwanted biases associated with methods based on stellar kinematics or spatial distributions. To complement this analysis, we also explore the distribution of disc stars from the Schuster et al. (2006) catalog.

The paper’s outline is as follows. Section 2 presents a brief review of the main properties of ringing. In Section 3 we describe the stellar samples analysed in this work. The distribution of stars in energy and angular momentum space of the F/G-dwarf and the Schuster et al. (2006) catalogs are analysed in Section 4 and 5, respectively. In Section 6 we apply the same analyses to high-resolution N-body simulations of the interaction between Sagittarius and the Milky Way. A summary and conclusions are presented in Section 7.

2 RINGING IN GALACTIC DISCS

Minchev et al. (2009), followed by Gómez et al. (2012, hereafter G12), showed that relatively massive minor-merger events can generate substructure in the velocity field of disc stars located in the Solar neighbourhood. Merging satellite galaxies with total masses as small as 10% of the mass of the Milky Way may excite density waves whose signatures can be identified even 5 Gyr after the first satellite’s pericentre passage. The space of E - L_z is particularly well-suited to identify density waves, since the waves are surfaces of constant energy (see also e.g. Helmi & de Zeeuw 2000; Helmi et al. 1999). Over time, these constant-energy features associated with the density waves become more closely spaced, and their number increases as a consequence of phase wrapping (see Section 3 of G12). In the top panel of Figure 1 we show, in E - L_z space, the distribution of disc particles located within a Solar neighbourhood-like sphere of 2.5 kpc radius, obtained from one of the simulations analysed in G12. The sphere is centred at 8 kpc from the galactic centre and the distribution was obtained after 3.9 Gyr of evolution, which corresponds to a time since total disruption of the satellite galaxy of 1.9 Gyr. In this simulation, the satellite galaxy has a total initial mass equal to 20% of the mass

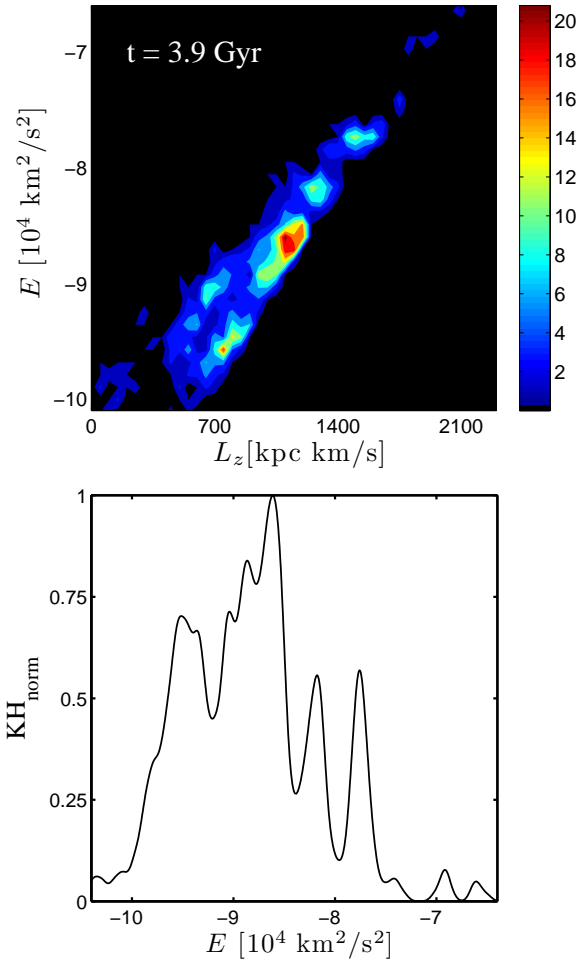


Figure 1. Top panel: $E - L_z$ distribution of disc particles inside a sphere of 2.5 kpc radius located at 8 kpc from the galactic centre, obtained from a simulation with a mass ratio of $M_{\text{host}}^{\text{total}}/M_{\text{sat}}^{\text{total}} = 0.2$. The total number of particles enclosed within this volume is $N_{\text{part}}^{\text{model}} = 976$. The snapshot corresponds to a time of 3.9 Gyr after the satellite was launched, or to 1.9 Gyr after the satellite fully merged with the host galaxy. The different colours (contours) indicate different number of particles. Note the large number of lumps with nearly constant energies associated with density waves crossing the sphere. Bottom panel: Kernel histogram (KH) of energies, E , obtained from the same distribution of particles. Each peak in the kernel histogram corresponds to a density wave observed in the top panel.

of the host. Note that only $N_{\text{part}}^{\text{model}} = 976$ are located within this 2.5 kpc sphere. It is clear that disc particles are distributed in different lumps of nearly constant energy, each of them associated with a different density-wave crossing. The bottom panel of Figure 1 shows a Kernel Histogram (KH) of energies, E . To compute the kernel histogram, a Gaussian kernel with bandwidth $\sigma = 0.011 \Delta E$ was assigned to each particle. Here, $\Delta E = 4 \times 10^4$ km 2 s $^{-2}$ is approximately the total extent of the satellite in energy space within this volume. The kernel histogram is the sum of all of the Gaussian kernels. Since density waves are surfaces of nearly constant energy, they are observed in the KH as well-defined peaks. Note that larger values of σ tend to oversmooth the KH, erasing some of the peaks associated with substructure observed in $E - L_z$ space. Conversely, smaller values produce

noisier KHs. In what follows we keep the values of σ and ΔE fixed at these values.

3 THE STELLAR SAMPLES

3.1 The SEGUE F/G-Dwarf sample

The SEGUE F/G-dwarf sample analysed in this work was culled from $\sim 70,000$ F and G type stars with available low-resolution spectroscopy ($R \sim 2000$), as provided in SDSS DR8 (Aihara et al. 2011). Among them, about 63,000 stars were targeted as G-dwarfs; hence, our sample is dominated by the G-dwarf candidates used by L11. The G-dwarf candidates were obtained by selecting stars with colours and magnitudes in the range $0.48 < (g - r)_0 < 0.55$ and $r_0 < 20.2$, respectively, while the rest of the sample covers $0.2 < (g - r)_0 < 0.48$, and $g_0 < 20.2$. Thanks to this simple selection function, the stellar sample is expected to be completely unbiased with respect to kinematics, and only slightly biased towards metal poor stars (see Schlesinger et al. 2009).

3.1.1 Local sample

In order to obtain a local sample of stars with accurate measurements of their 6D phase-space coordinates, as well as metallicities and $[\alpha/\text{Fe}]$ ratios, a series of cuts were applied to the complete catalog. Here we provide a brief summary of the criteria used for the sample selection, but we refer the interested reader to L11 for a more detailed description of this procedure as we follow their prescription to select the final sample.

Stellar atmospheric parameters, such as effective temperature, T_{eff} , surface gravity, $\log g$, and metallicity, $[\text{Fe}/\text{H}]$, were determined using the SEGUE Stellar Parameter Pipeline, SSPP (Lee et al. 2008a,b; Allende Prieto et al. 2008; Smolinski et al. 2011). In order to obtain high-quality estimates of both $[\text{Fe}/\text{H}]$ and $[\alpha/\text{Fe}]$ (Lee et al. 2011a), only stars with spectra of signal-to-noise ratios (S/N) greater than 30 \AA^{-1} were considered. Importantly, this also ensures that errors in the estimated radial velocities are smaller than 5 km s^{-1} . Proper motions were obtained following Munn et al. (2004), after correcting for the systematic error described in Munn et al. (2008). Distances to individual stars were estimated using calibrated set of stellar isochrones (An et al. 2009b), following the prescription of An et al. (2009a). To minimise possible distance bias from stellar age effects near the main sequence turnoff, only stars with $\log g \geq 4.2$ were considered. In addition, to minimise the errors on the estimates of phase-space coordinates, we only consider stars with distances from the Sun $0.4 \lesssim d \lesssim 2$ kpc. Note that the inner limit is imposed by the data itself, due to saturation of the SDSS photometric scans for $g \lesssim 14.5$.

To compute Galactocentric positions and velocities of our local stellar sample, we assume the Sun to be located at $R_{\odot} = 8$ kpc, and that it has a peculiar velocity with respect to the Local Standard of Rest (LSR) $(U, V, W)_{\odot} = (11.1, 12.2, 7.3) \text{ km s}^{-1}$ (Schönrich et al. 2010). We further assume a velocity of the LSR with respect to the Galactic centre of $V_{\text{LSR}} = 220 \text{ km s}^{-1}$. Finally, we discard stars with

$[\text{Fe}/\text{H}] \leq -1.2$ and $V_\phi < 0 \text{ km s}^{-1}$ in order to avoid contamination (as much as possible) from the stellar halo, as well as the proposed metal-weak thick-disc component of the Galaxy (Carollo et al. 2010).

3.1.2 The thin- and thick-disc populations

As mentioned in the Introduction, signatures of ringing are expected to be stronger in the thick disc than the thin disc because its stars are less affected by perturbations from the Galactic bar, self-gravitating spiral arms, and giant molecular clouds. More importantly, the thick disc is mainly composed of a very old stellar population, with ages of $\sim 10 - 12$ Gyr (Schuster et al. 2006; Bensby et al. 2007). Thus, most of its stars must have been in place as recently as 5 Gyr ago – a required condition if, for example, we seek to identify signatures of a merger event that may have started approximately at that time.

Following L11, we split our local sample into likely thin- and thick-disc populations on the basis of their stellar chemical abundances, i.e., $[\alpha/\text{Fe}]$ and $[\text{Fe}/\text{H}]$. We assign stars to the thin-disc (low- $[\alpha/\text{Fe}]$) and thick-disc (high- $[\alpha/\text{Fe}]$) components according to the following scheme:

For stars with $[\text{Fe}/\text{H}] \geq -0.8$

- thin disc, if $[\alpha/\text{Fe}] < -0.08 \cdot [\text{Fe}/\text{H}] + 0.15$
- thick disc, if $[\alpha/\text{Fe}] > -0.08 \cdot [\text{Fe}/\text{H}] + 0.25$

For stars with $[\text{Fe}/\text{H}] < -0.8$

- thin disc, if $[\alpha/\text{Fe}] < +0.214$
- thick disc, if $[\alpha/\text{Fe}] > +0.314$

While any old stellar population with high velocity dispersion would be suitable for our investigation, by assigning stars to the different components of the disc according to $[\alpha/\text{Fe}]$ we avoid introducing unwanted biases associated with methods based on stellar kinematics or spatial distributions. Note the gap of 0.1 dex left in the $[\alpha/\text{Fe}]$ cuts between the thin disc and thick disc, which is chosen to avoid misclassification of stars. For a detailed description of the motivation behind this scheme, we refer the reader to section 3.1 of L11.

3.2 The Schuster et al. (2006) sample

The Schuster et al. (2006, hereafter SCH06) catalog comprises a total of 1533 high-velocity and metal-poor stars. Positions and proper motions for these stars were primarily derived from Hipparcos (Perryman et al. 1997), Tycho-2 (Høg et al. 2000), and the revised NLTT catalog (Salim & Gould 2003), whereas radial velocities were obtained from a number of different sources available in the literature (see SCH06, and references therein). As in Section 3.1, we compute Galactocentric velocities by assuming $R_\odot = 8 \text{ kpc}$, $(U, V, W)_\odot = (11.1, 12.2, 7.3) \text{ km s}^{-1}$ and $V_{\text{LSR}} = 220 \text{ km s}^{-1}$.

Metallicities estimated via a photometric calibration based on *uvby-β* photometry are also provided for the entire sample. As shown by SCH06, it is possible to discriminate stars from different Galactic components by means of the X parameter, where X is a simple linear combination of the rotational velocity and metallicity of the stars. Following SCH06, we discard from our sample all stars with $X \geq 0$,

Table 1. Parameters of the present day Milky Way-like potential used in this work. Masses are in M_\odot and distances are in kpc.

Disc	Bulge	Halo
$M_d = 4 \times 10^{10}$	$M_b = 8 \times 10^9$	$M_{\text{vir}} = 1 \times 10^{12}$
$r_a = 6.5$	$r_c = 0.7$	$r_s = 21.5$
$r_b = 0.26$		$c = 12$

in order to avoid potential contamination from the Galactic halo¹.

Note that estimates of $[\alpha/\text{Fe}]$ are not provided in the SCH06 catalog. Thus, a subdivision between likely thin- and thick-disc stars cannot be performed following the scheme described in Section 3.1.2. Nevertheless, as shown by Nissen & Schuster (1991) and SCH06, the thin-disc population in this sample belongs to a very old disc component, with the bulk of the population older than 10 Gyr, and the remaining stars with ages between 10 and 4 Gyr. We thus ensure that most of these stars were already part of the disc ~ 5 Gyr ago. It is important to note that all disc stars in this sample are located at a distance from the Sun $d < 0.2 \text{ kpc}$. Thus, this sample probes the innermost regions of the Solar neighbourhood, complementing the more distant SDSS F/G-dwarf sample.

4 THE SEGUE F/G-DWARF SAMPLE IN $E - L_z$ SPACE

We now analyse the $E - L_z$ distribution of the stars present in our local SEGUE F/G-dwarf sample. In order to obtain an estimate of the orbital energy of these stars we first need to assume a shape for the Galactic potential. We adopt a model consisting of three different components. These are: (1) a Miyamoto-Nagai disc (Miyamoto & Nagai 1975)

$$\Phi_{\text{disc}} = -\frac{GM_d}{\sqrt{R^2 + (r_a + \sqrt{Z^2 + r_b^2})^2}}, \quad (1)$$

(2) a Hernquist bulge (Hernquist 1990),

$$\Phi_{\text{bulge}} = -\frac{GM_b}{r + r_c}, \quad (2)$$

and (3) a NFW dark matter halo (Navarro, Frenk & White 1996)

$$\Phi_{\text{halo}} = -\frac{GM_{\text{vir}}}{r [\log(1 + c) - c/(1 + c)]} \log\left(1 + \frac{r}{r_s}\right). \quad (3)$$

Table 1 summarises the numerical values of the parameters used for our Galactic potential model. These parameters are similar to those used by other authors (e.g., Bullock & Johnston 2005; Gómez et al. 2010; Peñarrubia et al. 2010) and fit the Milky Way rotation curve (Klypin et al. 2002). Note that, as described by Gómez & Helmi (2010, and references therein), the results are not strongly dependent on the particular choice of the potential, since substructure in integrals of motion space are

¹ Note that only a fraction smaller than 3% of our final F/G-dwarf thick-disc subsample has $X \geq 0$.

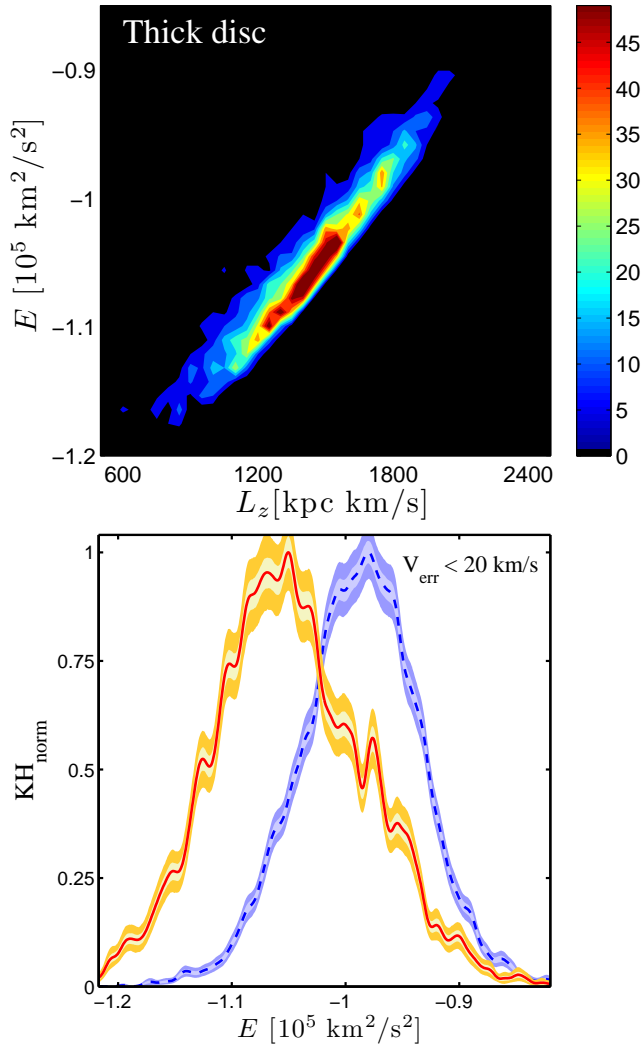


Figure 2. Top panel: $E-L_z$ distribution of likely thick-disc stars located within 2 kpc of the Sun, obtained from our F/G-dwarf sample. The different colours (contours) indicate different number of stars. Only stars with total errors in velocity $V_{\text{err}} < 20 \text{ km s}^{-1}$ are considered. The subsample contains $N_{\text{stars}}^{\text{thick}} = 3141$ high- $[\alpha/\text{Fe}]$ stars. Note the presence of a series of high-density features, especially at large values of energies. Bottom panel: kernel histogram of E , obtained from both the thick-disc (red solid line) and the thin-disc (blue dashed line) stellar subsamples. The thin-disc subsample contains $N_{\text{stars}}^{\text{thin}} = 4903$ low- $[\alpha/\text{Fe}]$ stars. The shaded areas indicate errors associated with poor sampling of the underlying distributions (see text). The high-density features observed in the top panel correspond to peaks in the kernel histogram. Note that the thin-disc subsample exhibits a smoother distribution relative to the thick disc.

robust to small differences in the mass distribution because we always focus on small volumes in space. Hence, small changes in the potential essentially act as a zero-point offset, affecting all the stars present in this volume in the same way.

4.1 Thin vs. Thick disc

The top panel of Figure 2 shows the distribution of α -enhanced, likely thick-disc stars in $E-L_z$ space. For this

figure we have only considered stars with $d \leq 2$ kpc from the Sun and a total velocity error $V_{\text{err}} < 20 \text{ km s}^{-1}$. As a result, and because of the different cuts applied to the complete catalog (see Section 3.1), we are only left with a total of $N_{\text{stars}}^{\text{thick}} = 3141$ likely thick-disc stars. A series of high-density features can be observed in this panel, especially at high values of E and L_z . These features become more evident in the kernel histogram of energies, shown as a red solid line in the bottom panel of the same figure. Comparison with Figure 1 clearly indicates that, if these features are to be associated with ringing, they have a much smaller amplitude than might be expected. However, due to the relatively large threshold in total velocity errors considered (i.e., $V_{\text{err}} < 20 \text{ km s}^{-1}$), these peaks may have been smoothed out; we explore this issue further in Section 4.2. On the other hand, due to the relatively low number of stars, some of the peaks may have arisen due to noise associated with poor sampling of the underlying distribution. To investigate this, we bootstrapped our thick-disc stellar subsample 2000 times and computed a kernel histogram for each one of the realisations. At each value of E , we sort the results of the KHs in ascending order. The shaded areas in the bottom panel of Figure 2 show the 25-75 percentiles (light shadow) and the 5-95 percentiles (dark shadow) of the distribution of values obtained from the bootstrapped KHs. The results of this procedure indicate that only a few of these peaks have amplitudes with values above the noise level. However, in the following sections we show that, after accounting for the effects of measurement errors, and through exploration of the SCH06 catalog, some of the remaining peaks may indeed be real.

The bottom panel of Figure 2 also shows (blue dashed line) the kernel histogram on E of the stars associated with the low- α , likely thin-disc stars. In this case, the total number of stars in the subsample is $N_{\text{stars}}^{\text{thin}} = 4903$. It is very interesting to observe that the distributions associated with the thin disc and thick disc are shifted with respect to one another. The thin-disc subsample comprises a population of stars that, at least locally, is less tightly bound than that of the thick disc. Note that, within volumes as small as the ones considered here, the Galactic potential can be regarded as constant. Thus, for these stars, the binding energy is mainly a function of their velocities. Since the thick disc is composed of a population of stars with a lag in V_ϕ of $\sim 30 \text{ km s}^{-1}$ relative to the thin disc (as shown in, e.g., L11), it is not surprising to find that these stars have a larger binding energy². It is also noticeable that the thick-disc stars exhibit a much broader distribution in energy than their thin-disc counterparts. This is a manifestation of the larger velocity dispersion (in all directions) associated with the thick-disc component. Finally, note that the thin disc exhibits a much smoother distribution when compared to that of the thick disc. One has to bear in mind that the thin-disc subsample is also $\sim 35\%$ larger than the thick-disc subsample. Thus, noise associated with poor sampling is reduced. This is indicated by the tighter blue and light-blue shaded regions, computed as discussed above. Nevertheless, in Section 4.2 we show

² Note that the mean radial and vertical velocity components for both populations are $\sim 0 \text{ km s}^{-1}$.

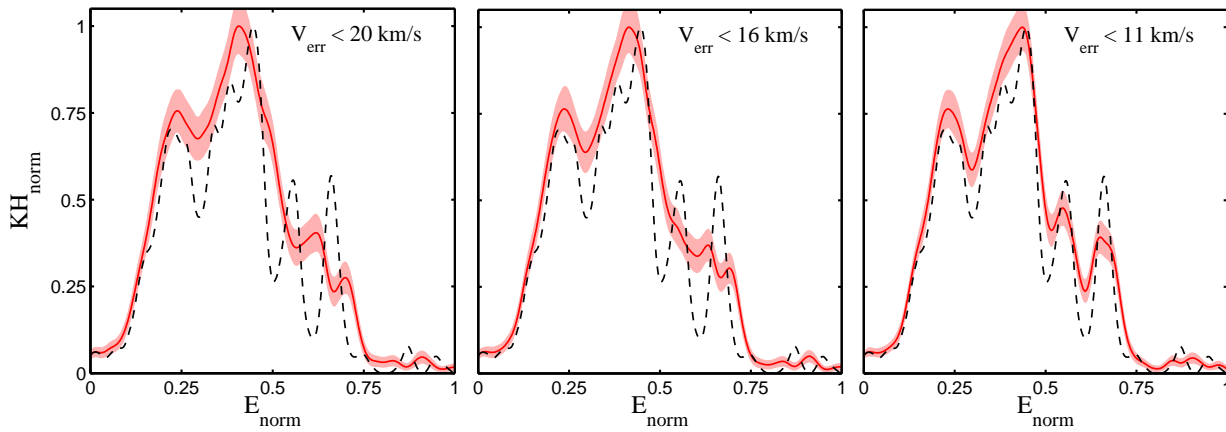


Figure 4. Kernel histograms of normalised energies, obtained from the distribution of particles shown in Figure 1, after convolving with measurement errors. The red solid line in each panel shows the averaged kernel histogram obtained after 400 realisations of the error convolution. The maximum error in total velocity considered is indicated in the top right corner of each panel. The shaded regions indicate 1σ deviations from the mean. For comparison we show, with a dashed black line, the kernel histogram obtained from the same distribution of particles before convolution. When errors in total velocity as large as 20 km/s are considered, most of the peaks in the histogram are erased (left panel). These peaks are recovered when we reduce the magnitude of the maximum error to 11 km/s (right panel).

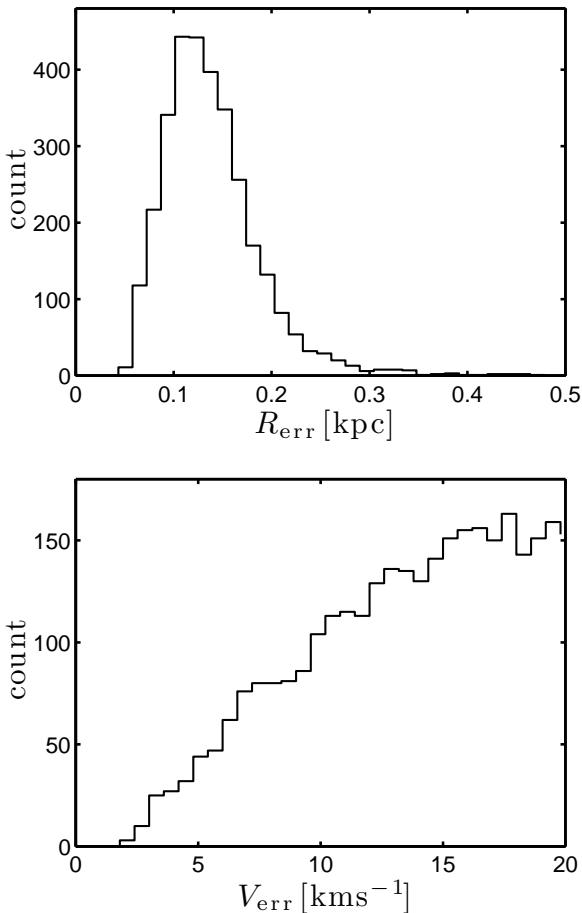


Figure 3. Distribution of total errors in positions (top panel) and velocities (bottom panel), extracted from our likely thick-disc SDSS F/G-dwarf subsample.

that this result holds even when considering smaller stellar subsamples with more accurately determined velocities.

4.2 Characterising the effects of errors on phase-space coordinates

As noted above, the measurement errors in the phase-space coordinates of our local F/G-dwarf stellar sample may be large enough to either smooth out or erase some of the signatures of ringing in $E - L_z$ space. To characterise their effect on the observed features in the kernel histograms, we have extracted the distributions of errors from our thick-disc subsample, and convolved them with the position and velocities of the particles shown in Figure 1. Estimates of the errors were obtained from the SSPP (see L11 and references therein); their distributions are shown in Figure 3. The left panel of Figure 4 shows the results of this convolution when errors in velocities as large as 20 km^{-1} are considered. The red solid line shows the averaged kernel histogram of normalised energies, E_{norm} , obtained after 400 different realisations of the error convolution, whereas the shaded region indicates its standard deviation. Here, $E_{\text{norm}} = (E_i - \min(E))/\Delta E$, with ΔE defined as in Section 2. It is important to remark that, to compute the energies of the N -body particles after convolution with errors, we have used the same analytic potential that was used for the F/G-dwarf sample. Note that this simulation was designed to emulate the result of a minor merger experienced by a Milky Way-like galaxy at $z = 1$. Thus, the properties of this potential were scaled to those expected at $z = 1$, as described in Section 2 of G12. Interestingly, due to the large magnitude of the errors considered, most of the structure associated with ringing has been erased. Furthermore, some spurious peaks can be observed. For comparison we show with a black dashed line the kernel histogram obtained from this set of particles before error convolution. The middle panel of this figure shows the results of the same procedure, now after convolving with errors in velocity $V_{\text{err}} < 16 \text{ km}$

s^{-1} . Note that these errors are still large enough to erase most of the signatures of ringing. Only when considering errors in velocity $V_{\text{err}} < 11 \text{ km s}^{-1}$ (right panel) do we start recovering the previously-observed peaks.

This exercise clearly indicates that, in order to detect signatures of ringing in the Milky Way disc, very accurate 6D phase-space catalogs must be explored. A highly accurate subset of stars can be obtained from our local F/G-dwarf sample, at the expense of significantly reducing the total number of stars analysed. The top panel of Figure 5 shows the kernel histograms of the thick disc (red solid line) and the thin disc (blue dashed line) obtained when only stars with total velocity errors $V_{\text{err}} < 11 \text{ km s}^{-1}$ are considered. As a result of this more restrictive cut, we are left with $N_{\text{stars}}^{\text{thick}} = 968$ thick-disc and $N_{\text{stars}}^{\text{thin}} = 1132$ thin-disc stars, respectively. Interestingly, not only do we recover most of the features already observed in Figure 2, but also structure here is more sharply defined (as expected from our previous discussion). Note, however, that errors associated with poor sampling of the underlying distribution are larger due to the smaller number of stars. This is evident by the wider areas covered by the shaded regions, obtained from the bootstrap analysis of our subsample (see Section 4.1). Nevertheless, it is important to note that the number of thick-disc stars in this more accurate subsample, $N_{\text{stars}}^{\text{thick}}$, is approximately equal to the number of particles analysed in the N -body model, $N_{\text{part}}^{\text{model}}$, shown in Figures 1 and 4.

Alternately, it is possible to obtain a more accurate subsample simply by analysing a much more local subset of stars. In the bottom panel of Figure 5 we show the kernel histogram of E obtained from a sample of stars with heliocentric distances projected onto the plane $R \leq 0.5 \text{ kpc}$. Note that by reducing the radius of our Solar neighbourhood sphere we are not only constraining errors in the velocities of the stars, but also in their positions. After the cut we obtain a thick-disc subsample of $N_{\text{stars}}^{\text{thick}} = 2441$ stars, whereas the thin-disc subsample contains $N_{\text{stars}}^{\text{thin}} = 3021$ stars. Comparison with the top panel of Figure 5 and Figure 2 shows again that many previously-observed features are preserved. Furthermore, some of the features have become *even more significant*, in particular, the peak located at $E \approx -0.97 \times 10^5 \text{ km}^2 \text{ s}^{-2}$. It is also interesting to note that, as previously discussed in Section 4.1, the thin-disc population exhibits a smoother energy distribution relative to that of the thick-disc population in both of these panels. Notice that now both subsamples have comparable numbers of stars.

5 THE SCHUSTER ET AL. (2006) SAMPLE IN $E - L_Z$ SPACE

The previously-observed peaks in the kernel histograms of our SEGUE F/G-dwarf sample might be an indication of ringing in our own Galactic thick disc. However, due to the relatively small number of stars with the necessary small measurement errors, uncertainties associated with poor sampling of the underlying distribution are (for some features) still large. It is therefore important to look for additional evidences of ringing in other stellar catalogs already available in the literature. The SCH06 is particularly well-suited for this analysis, as it comprises a set of old and metal-poor disc stars (see Section 3.2). Furthermore, the disc stars in

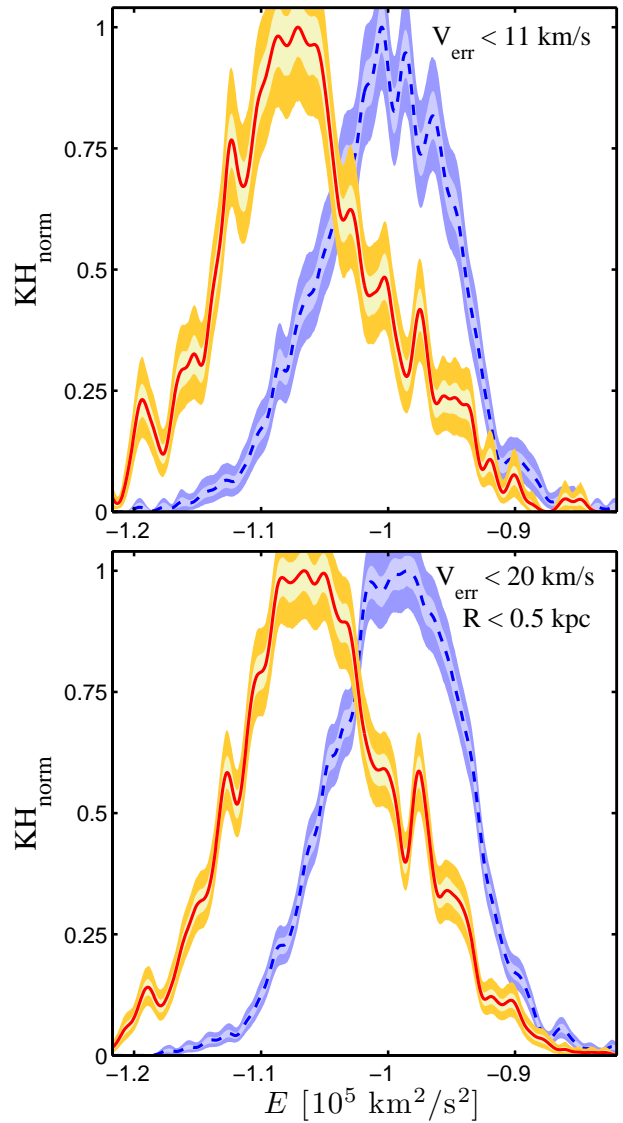


Figure 5. Top panel: Kernel histograms of energies obtained from the SEGUE F/G-dwarf thick disc (red solid line) and the thin disc (blue dashed line), when errors in total velocity smaller than 11 km/s are considered. The shaded regions indicate errors associated with poor sampling of the underlying distribution (see Section 4.1). Note that most of the previously-observed features in Figure 2 are more sharply defined, as expected from this more accurate subsample. Note as well that the thin disc presents a smoother distribution in E_{norm} with respect to the thick disc. Bottom panel: As above, for stars located within $R \leq 0.5 \text{ kpc}$ and total velocity errors smaller than 20 km/s .

this sample are all located within $d < 0.2 \text{ kpc}$, thus they probe a region of the Solar neighbourhood that is different than that explored by the more distant SEGUE F/G-dwarf sample.

The black dashed line on the top panel of Figure 6 shows the kernel histogram obtained from a subsample of likely disc stars from the SCH06 catalog. Following our previous discussion, we first consider stars with total errors in velocities $V_{\text{err}} \leq 11 \text{ km s}^{-1}$. As a consequence, we are left with a total of 603 old disc stars. Interestingly, a large number of peaks can be observed, most of them located at values

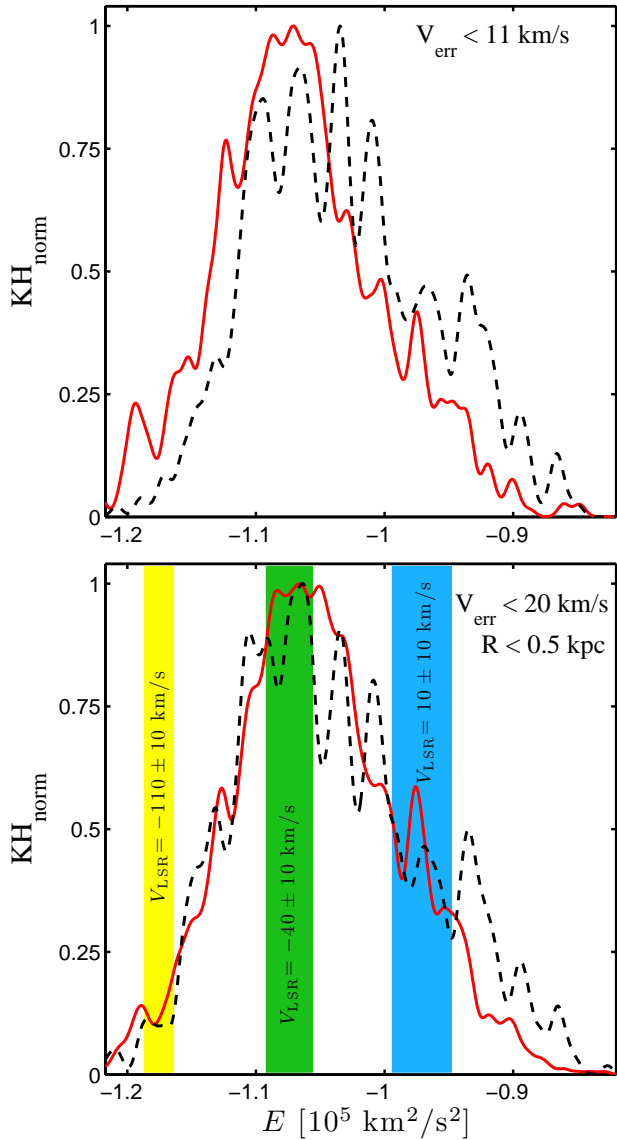


Figure 6. Top panel: Kernel histogram of E obtained from the SCH06 sample of disc stars with total velocity error $V_{\text{err}} < 11$ km/s, shown with a black dashed line. The sample contains a total of 603 stars. Note the large number of peaks located at very similar values of E as in the kernel histogram of the F/G-dwarf subsample, indicated with a red solid line. The slight shift between these two distributions can be accounted for by the different volumes probed by the samples (see text), as well as poor sampling of the underlying energy distribution. Bottom panel: As in the top panel, for a sample of disc stars with total velocity error $V_{\text{err}} < 20$ km/s. This larger sample contains 813 stars. The coloured areas indicate the approximate energy range of the Arcturus stream (yellow), the Hercules stream (green), and the most significant peak identified in the SEGUE F/G-dwarf sample (light blue).

of E consistent with those observed in the kernel histogram of F/G-dwarf subsample, shown with a red solid line. As we explain in Section 6.2, due to the strong radial and azimuthal dependence on the location and amplitude of the peaks, together with the poor sampling of the underlying energy distribution, it is not surprising to find features in

these kernel histograms slightly shifted with respect to one another.

The bottom panel of Figure 6 shows the kernel histogram from the SCH06 catalog, obtained after considering stars with total velocity errors of $V_{\text{err}} \leq 20$ km s⁻¹. This larger sample contains 813 stars. Again, note that many of the features observed in the KHs of both the SCH06 and the F/G-dwarf samples are located at very similar values of E . The colour-coded areas in this panel indicate the approximate energy range in which the Arcturus and the Hercules moving groups are expected to be found. To compute these energy ranges, for simplicity, we have assumed for each moving group:

- a characteristic V velocity component, V_{LSR} (see, e.g., Dehnen 1998; Fux 2001; Antoja et al. 2008; Navarro, Helmi & Freeman 2004; Klement, Fuchs & Rix 2008). Since this characteristic V velocity is subject to relatively large uncertainties, to compute each energy range we assumed $V = V_{\text{LSR}} \pm 10$ km s⁻¹
- a characteristic U velocity component equal to zero
- a Galactocentric distance $R = 8$ kpc

The bottom panel shows that both moving groups could be associated with peaks in our KH. Note that, as previously explained in this Section, it is not surprising to find slight shifts in the location of the peaks between the two analysed samples due to the different volumes probed. M09 considered the possibility that the Arcturus moving group is the result of a perturbation in the Galactic disc induced by a minor merger event. They concluded that a minor merger that took place ~ 1.9 Gyr ago could explain not only the presence of the Arcturus moving group, but also other previously observed features in the local velocity field (see e.g. Arifyanto & Fuchs 2006). It is important to note that streams with velocities larger than $V_{\text{LSR}} \sim \pm 50$ km s⁻¹ are less likely to be related to the Galactic bar. Interestingly, the short timescale associated with this event is consistent with the estimated age of the Galactic bar, as measured by Cole & Weinberg (2002) (< 3 Gyr ago). This suggests that the same event that could have caused the formation of the Galactic bar could have also left the stellar disc unrelaxed, thus giving rise to the observed high-velocity stream. On the other hand, many studies have successfully described the presence of the Hercules moving group as a result of a resonant interaction with the bar (see e.g. Dehnen 2000; Minchev et al. 2007). However, as shown by Antoja et al. (2009, 2011), the effect that bars and spiral density waves have on the velocity field of galactic discs is highly degenerate³. Therefore, the scenario in which the Hercules moving group was formed as the response of the Galactic disc to a minor merger event cannot be ruled out.

6 THE SAGITTARIUS DWARF GALAXY AS A POSSIBLE PERTURBER

The impact that the Sagittarius dwarf galaxy may have had on the Galactic disc has been previously considered by several authors. Recently, using high-resolution N -body

³ Note that both mechanisms could be acting simultaneously.

Table 2. Initial properties of the two N -body simulations analysed in Section 6.

Host			
DM halo	$N_{\text{part}} = 2.65 \times 10^7$		
Virial mass	1×10^{12}	$[M_{\odot}]$	
Scale radius	14.4	[kpc]	
Stellar disc			
$N_{\text{part}} = 3 \times 10^6$			
Mass	3.59×10^{10}	$[M_{\odot}]$	
Scale length	2.84	[kpc]	
Scale height	0.43	[kpc]	
Stellar bulge			
$N_{\text{part}} = 5 \times 10^5$			
Mass	9.52×10^9	$[M_{\odot}]$	
Effective radius	0.56	[kpc]	
Sérsic index	1.28		
Satellites			
DM halo	<i>Light</i>	<i>Heavy</i>	$N_{\text{part}} = 1.8 \times 10^6$
Virial mass	0.32×10^{11}	1×10^{11}	$[M_{\odot}]$
Scale radius	4.9	6.5	[kpc]
Stellar spheroid			
$N_{\text{part}} = 5 \times 10^4$			
Core radius	1.5	1.5	[kpc]
Tidal radius	4	4	[kpc]
Central vel. disp.	23	30	[km s $^{-1}$]

simulations, P11 showed that its gravitational interaction may play a significant role on shaping the morphology of the Galactic disc, by inducing the formation of rings, influencing the Galactic bar, and flaring the outer disc. Its interaction could also explain the formation of the Monoceros rings (Newberg et al. 2002; Quillen et al. 2009; Michel-Dansac et al. 2011; Purcell et al. 2011). However, until now, its influence on the phase-space distribution of disc stars located within the neighbourhood of the Sun has not been explored. In this section we analyse the simulations presented by P11 to characterise the effect of Sagittarius within this volume.

6.1 The simulations

Two simulations with different models for the Sagittarius dwarf galaxy progenitor were performed. In both cases, the primary galaxy includes a NFW dark matter (DM) halo, an exponential stellar disc and a central bulge following a Sérsic profile. The *Light Sgr* and *Heavy Sgr* progenitors were self-consistently initialised with a NFW DM halo and a separate stellar component following a King profile (King 1966). Table 2 summarises the numerical values of the parameters used for these models. Following previous work on the Sgr interaction (Keselman, Nusser & Peebles 2009), the satellites were launched at 80 kpc from the galactic centre in the plane of the Milky Way, traveling vertically at 80 km s $^{-1}$ toward the north galactic pole. The simulations reach a present day configuration after approximately 2.7 and 2.1 Gyr of evolution, respectively. Mass loss that would have occurred between virial radius infall and this “initial” location is accounted for by truncating the progenitor DM halo mass

profile at the instantaneous Jacobi tidal radius, $r_t = 23.2$ and 30.6 kpc, respectively. This leaves a total bound mass that is a factor of ~ 3 smaller than their effective virial mass originally assigned. Each of the model Sgr progenitors experiences two disc crossings, approaching a third at the present day. The satellite first crosses the disc at a galactocentric distance of ~ 20 kpc approximately ~ 1.75 Gyr ago, producing the most significant perturbation. The progenitor loses roughly 75% of its dark matter mass (but little stellar material) during this time. In the bottom panel of Figure 7 we show the time evolution of the satellites’ galactocentric distance. The initial disc in both Sgr-infall models is completely smooth at $t = 0$ Gyr, and only develops a mild bar when it is evolved in isolation for a few Gyr. When compared to the isolated run, the *Light Sgr* model results in a stronger bar (see P11). Conversely, as a result of enhanced central disc heating, the more massive satellite suppresses bar formation. The endstate bar orientation, $\phi_{\text{bar}}^{\text{sim}} = 15^\circ - 20^\circ$, is in both cases consistent with estimates of the long bar’s orientation observed in the center of the Milky Way, $\phi_{\text{bar}}^{\text{MW}} = 15^\circ - 30^\circ$ (Bissantz & Gerhard 2002). The simulations used the parallel N -body tree code ChaNGa (Gioachin et al. 2007), with a gravitational softening length of one parsec 4 , and followed the evolution of 30 million particles with masses in the range $1.1 - 1.9 \times 10^4 M_{\odot}$.

6.2 The phase-space distribution of Solar neighbourhood-like volumes

We now characterise the phase-space distribution of particles within Solar neighbourhood-like volumes of 1 kpc radii. In these simulations, according to the location of the Sagittarius remnant and its tidal debris, the Sun should be located at approximately $(0, -8, 0)$ kpc from the galactic centre. In order to examine the dependencies of the particle’s phase-space distribution with azimuthal angle, and uncertainties on the location of the “Sun” associated with the model, we have placed 5 spheres at different azimuthal angles, covering a total of $\approx 58^\circ$ around the “Sun.” The top panel of Figure 7 shows contour plots of the final distribution of particles in the X - Y plane obtained from the *Heavy Sgr* simulation. The white dots trace the regions where Sgr crosses the plane of the disc and its current projection on the X- Y plane. The locations of our Solar neighbourhood spheres are indicated with solar symbols. As shown by P11, the gravitational interaction between the Sagittarius-like satellite and the galactic disc is sufficiently strong to induce the formation of transient spiral arms or rings. These arms can be clearly observed outside a radius of 15 kpc, but not so clearly at the Solar radius. In the top panels of Figure 8 we show the kernel histograms of E obtained from the distribution of particles located within these volumes. Let us recall that throughout this work we have kept fixed both the value of ΔE and the value of the bandwidth of the Gaussian kernel, σ . The black solid lines show the results obtained when the particle energies are computed using the analytic potential introduced in Section 4, whereas for the red dashed lines energies were computed directly from

⁴ The force softening length is set to roughly 0.1 of the mean disc interparticle spacing.

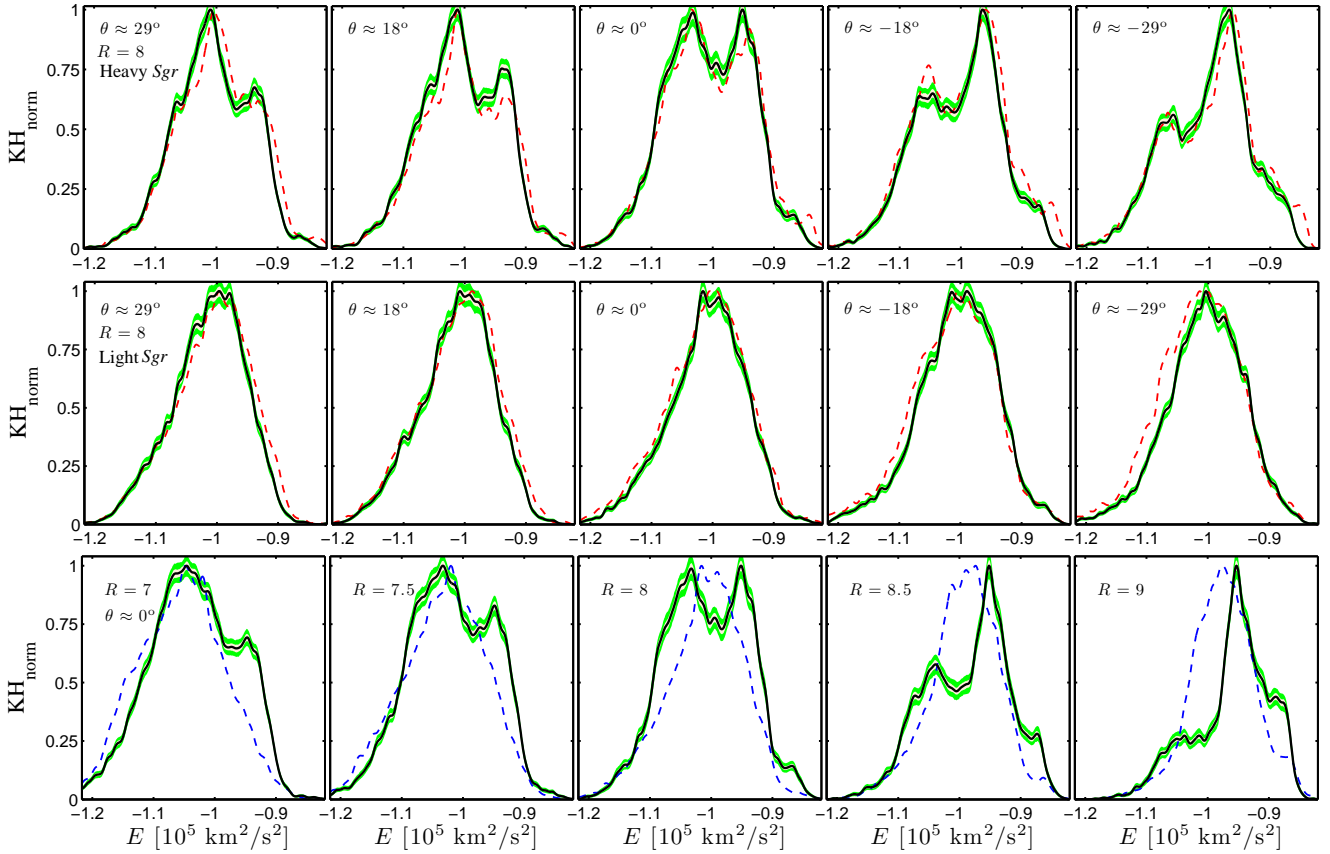


Figure 8. Top panel: Kernel histograms of energies obtained from the *Heavy Sgr* simulation. Each panel shows the kernel histogram (KH) obtained from the distribution of particles within a Solar neighbourhood sphere located at a different galactocentric azimuthal angle, θ . The black solid lines show KHs obtained after computing particle’s energy using the analytic potential described in Section 4. The red dashed lines show the KHs obtained after computing particle’s energies from the N -body potential. The shaded regions indicate errors associated with poor sampling of the underlying distribution (see Section 4.1). The angle θ is measured clockwise, starting from the negative Y axis in Fig. 7. The azimuthal location of the spheres are indicated in the top left corner of each panel. Note that all the KHs exhibit multiple peaks associated with density waves crossing the Solar neighbourhood-like volumes. Furthermore, the locations of these peaks strongly depend on the azimuthal location of the sphere. Note as well the good agreement between the second panel ($\theta \approx 18^\circ$) and the KHs obtained for our F/G-dwarf thick-disc subsample shown in Figures 2 and 5. Middle panels: As above for the *Light Sgr* simulation. Note that, as expected for a less-massive satellite, the peaks previously observed on the KHs of the *Heavy Sgr* model are either very mild or not present at all. Bottom panels: As above, now for spheres located at a different galactocentric radius, R . The spheres are located at an azimuthal angles $\theta = 0^\circ$. The galactocentric distance of the spheres are indicated in the top left corner of each panel. The black solid and blue dashed lines show the KHs obtained from the *Heavy Sgr* and *light Sgr* simulations, respectively. For the *Heavy Sgr* simulation, the locations and amplitude of the peaks in the KHs strongly depend on the radial position of the spheres. Note as well the similarities between the second panel ($R = 7.5$ kpc) and the KHs obtained for our F/G-dwarf thick-disc subsample. For the *Light Sgr* simulation, mild signatures of density waves can be observed only in the outer spheres, where the perturbation from the satellite galaxy is stronger.

the N -body potential. The very good agreement between the two KHs reflects the weak dependence of the amount and distribution of features with the particular choice of the galactic potential. Note that, for comparison, the red dashed lines have been slightly shifted in energy, so that both KHs overlap in the same energy range. On average, the number of particles contained in each sphere is $\approx 10,000$. It is interesting to observe that all the analysed volumes exhibit peaks in their KHs; these are features associated with density waves. We see strong dependence of the distribution and amount of peaks with azimuthal angle, θ : as θ is decreased, power from the highest amplitude peak ($E \approx -1.01 \times 10^5 \text{ km}^2 \text{ s}^{-2}$ at $\theta \approx 29^\circ$), or density wave, is transferred towards a secondary peak at higher energy ($E \approx -0.96 \times 10^5 \text{ km}^2$

s^{-2} at $\theta \approx -29^\circ$). In addition, the location of each peak is shifted towards lower values of E indicating that, on average, these peaks are populated by more inner particles. This is the expected behaviour from a spiral pattern traveling in this angular direction (see also Section 4.2 of G12). Note the similarities between the KH in the second top panel of Figure 8 ($\theta \approx 18^\circ$) with the KHs obtained from our F/G-dwarf thick-disc subsample, shown in Figures 2 and 5. This result clearly indicates that some of the features observed in the KH of the Milky Way thick disc, especially the peak at $E \approx -0.97 \times 10^5 \text{ km}^2 \text{ s}^{-2}$, could be associated with density waves excited by the Sagittarius dwarf galaxy. An important implication of the strong azimuthal dependence observed in our simulations is that the orbital properties of the Sagit-

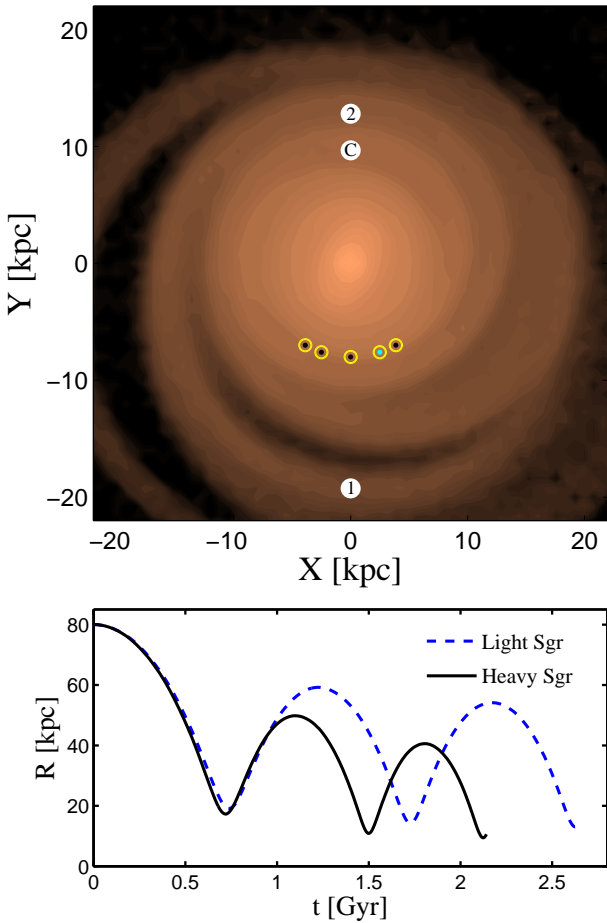


Figure 7. Top panel: Distribution of particles in the X - Y plane, as obtained from the *Heavy Sgr* simulation after approximately 2.1 Gyr of evolution. The different colours (contours) indicate different numbers of particles. As a consequence of the non-axisymmetrical energy kick imparted by the satellite, spiral features are induced in the galactic disc. The location of the Solar neighbourhood-like volumes analysed in Section 6.2 are indicated with solar symbols. The cyan dot indicates the local volume that best resembles the observations in the Solar Neighbourhood. The white dots labelled as “1” and “2” trace the regions where the *Heavy Sgr* crosses the plane of the disc for the first and second time, respectively. Its current projection on the X - Y plane is indicated with the symbol “C”. Bottom panel: Evolution of the galactocentric distance of both *Sgr* models as a function of time.

tarius dwarf galaxy could be further constrained by fitting the locations and amplitude of the significant peaks in the models to those observed in stellar samples.

In the middle panels of Figure 8 we show the results of the previous analysis obtained from the *Light Sgr* model. The Solar neighbourhood-like spheres were placed at the same locations. As before, the black solid lines show the kernel histograms obtained after computing particle energies using the analytic potential, whereas for the red dashed lines the *N*-body potential was used. As expected from a less-massive satellite (and thus a weaker perturber), the peaks previously observed in the kernel histograms of the *Heavy Sgr* model are either very mild or not present at all. It is interesting to note that, as previously discussed, the *Light Sgr* model results in a much stronger bar than the *Heavy*

Sgr model. The more massive satellite suppresses bar formation as a result of enhanced central disc heating. This clearly demonstrates that none of the observed features in these simulations could be associated to resonances with the galactic bar. Otherwise, we would expect to observe higher-amplitude features in the *Light Sgr* model’s kernel histograms as a result of the interaction with the stronger bar. Thus, models of the Sagittarius dwarf galaxy progenitor with a total mass $\leq 10^{10.5} M_{\odot}$ could be ruled out. Moreover, note that its total mass could be further constrained by comparing the amplitudes of the significant peaks observed in the kernel histograms of models with those of the Milky Way disc.

In the bottom panels of Figure 8 we explore Solar neighbourhood-like spheres of 1 kpc radius centred at different galactocentric distances. The spheres are separated by 0.5 kpc, and are all located at $\theta = 0^{\circ}$. The black solid lines show the kernel histogram obtained from the *Heavy Sgr* model. A strong dependence on the amplitude of each peak with galactocentric radius can be observed. As we move towards the galactic centre we better sample inner density waves, represented by peaks at lower energies. Again, note the similarities between the KHs obtained in the inner spheres (e.g., $R = 7.5$ kpc) and those obtained from our F/G-dwarf sample (see e.g. Fig. 5). The blue dashed lines in the bottom panels of Figure 8 show the KH obtained from the *Light Sgr* model. As expected, mild signatures of density waves can be observed only in the outer spheres, where the perturbation from the satellite galaxy is stronger. In Figure 9 we show the time evolution of the kernel histogram of particles located within a given Solar neighborhood-like sphere for ≈ 2.5 Gyr. To track this volume over time, our sphere is rotating with an angular frequency set by the velocity of the LSR, obtained after correcting the final mean rotational velocity profile for axisymmetric drift. The KH are shown at four different times: the initial conditions, the two pericentre passages, and the present day configuration. From this figure it is possible to appreciate the smooth distribution of particles in energy space at $t = 0$. In addition, it is possible to observe that strong perturbations in the disc particles energy distribution are only excited after the first pericentre passage of the *Heavy Sgr* satellite, as shown by the black solid line. Note that the smaller number of peaks in the KH of the *Heavy Sgr* model with respect to the KH shown in Figure 1 is due to the shorter period of time this simulation has been evolved. The blue dashed lines show KHs obtained from the *light Sgr* model. Notice the approximately smooth energy distribution at all times.

7 SUMMARY AND CONCLUSIONS

We have analysed the SEGUE F/G-dwarf and the Schuster et al. (2006) stellar samples in search for imprints of minor merger events in the Milky Way disc. In contrast to a number of previous studies, we look for perturbations in the phase-space of the host disc rather than merger remnants. We apply the same analyses to high-resolution *N*-body simulations of the interaction between the Sagittarius dwarf galaxy and the Milky Way. We summarise our results as follows:

- The alpha-enhanced, likely thick-disc F/G-dwarf subsample exhibits significant peaks in the stellar energy kernel

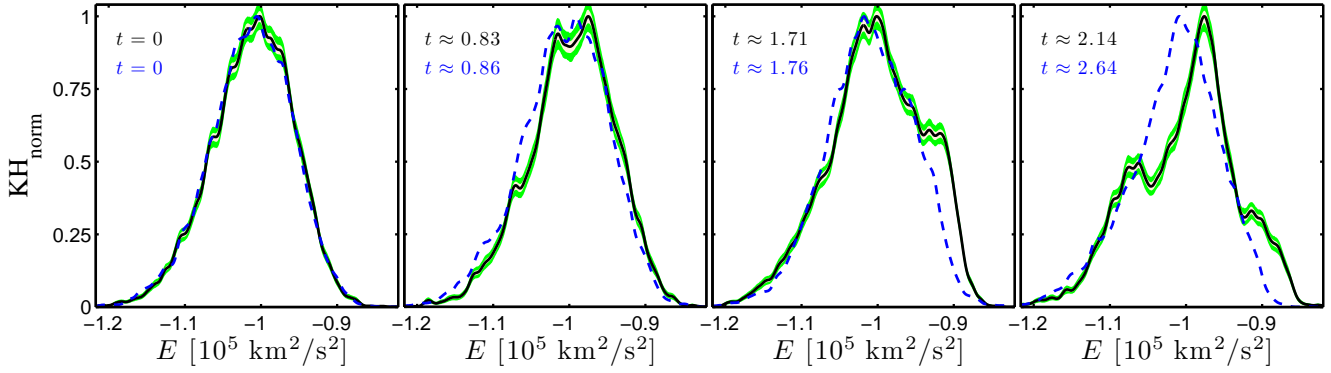


Figure 9. Kernel histograms of energies obtained from both Sgr simulations at different times. Each panel shows a KH obtained from a distribution of particles within a Solar neighbourhood-like sphere located at $R = 8$ kpc and rotating with an angular frequency set by the velocity of the LSR, after correcting for axisymmetric drift. The KH are shown at four different times: the initial conditions, the two pericentre passages and the present day configuration. The black solid lines show KHs obtained *Heavy Sgr* model. Note the smooth distribution of particles in energy space at $t = 0$. Strong perturbation in the disc particles energy distribution are only excited after the first pericentre passage of the satellite. The blue dashed line show the KH obtained from the *light Sgr* model. Note the approximately smooth energy distribution at all times.

histograms (KH). Conversely, the thin-disc subsample shows a much smoother distribution. This is consistent with the expectation that merger-induced perturbations in the host galaxy disc (e.g., the Milky Way) create structure in the stellar phase-space density, which survives until later times only in the old, hotter stellar population.

- We show that, to unambiguously identify merger-induced waves (ringing), samples of stars with velocity errors $V_{\text{err}} < 11 \text{ km s}^{-1}$ are required. This depends on the time since the waves were excited, as well as on the mass of the perturber.

- Complementary evidence of ringing can be obtained from the SCH06 catalog. The energy kernel histogram of stars here also reveals peaks, most of them remarkably consistent with those observed in the F/G-dwarf sample.

- Simulations of the interaction between the Milky Way and the Sagittarius dwarf galaxy show that a relatively-massive progenitor (i.e., masses of $\approx 10\%$ of the host) can induce density waves in the Galactic disc. Furthermore, the features seen in the energy kernel histogram of the observational data can be qualitatively well reproduced with these simulations. This is interesting since, by matching features in the kernel histograms of both models and observations, one could attempt to further constrain the orbital properties of Sagittarius, thanks to the strong azimuthal and radial dependence of the distribution of peaks. Note, however, that other possible origins for these perturbations need to be ruled out before performing this kind of analysis.

- On the contrary, low-mass models of Sagittarius barely excite density waves in the disc. Thus, if we assume that the observed peaks in the kernel histogram of the F/G-dwarf sample are the response of the Galactic disc to the tidal interaction with Sgr, we could rule out such low-mass models. Furthermore, by matching the amplitudes of the peaks, one could attempt to further constrain the total mass of the Sagittarius progenitor.

Comparing Figures 5 and 8, we note that variations in the azimuthal and radial positions of the Sun with respect to the Sagittarius orbital plane can result in similar

structure in the stellar energy distribution. This degeneracy can be broken by studying in detail the variation of features in the stellar phase-space distribution when position in the disc is varied. This in turn requires larger and deeper stellar samples, which will become available in ongoing and future surveys, such as APOGEE (Majewski et al. 2010), HERMES (Wylie-de Boer & Freeman 2010), and ultimately *Gaia* (Perryman et al. 2001).

Although we cannot fully discard the possibility that the observed features have some secular origin, the much smoother energy distribution of the thin-disc population make this scenario unlikely. If these features had originated by resonant interaction with, e.g., the Galactic bar, we would expect them to be stronger in the thin disc, rather than in the thick disc. This result is consistent with the hypothesis that features associated with ringing should last longer in the thick disc. Thick-disc stars spend relatively little time near the Galactic plane, where heating from spiral arms or the bar and scattering by giant molecular clouds is most vigorous. In addition, features generated by the bar or spiral arms can be observed as lumps in the u - v plane. We have explored this plane, and found no significant overdensities that could be linked to this kind of secular perturbations.

In this study we considered simulations with two different masses for the Sagittarius progenitor, representing a lower ($M_{\text{vir}} = 10^{10.5} M_{\odot}$) and upper ($M_{\text{vir}} = 10^{11} M_{\odot}$) limits. We have found that the *Light Sgr* cannot explain the structure seen in the energy distribution of our observed samples. On the other hand, the *Heavy Sgr* model creates strong disturbances in the Milky Ways disc, resulting in prominent peaks in the energy kernel histogram in localised spatial volumes, perhaps even stronger than what is seen in the observations (compare Figures 5 and 8). As shown by G12, satellites with masses 10% and 20% of the mass of their host generate density waves, which can be followed for no longer than 1 and 2 Gyr after the satellite’s full disruption, respectively. Close encounters between massive substructures and galactic discs should be common occurrences in a Λ CDM cosmology since $z = 1$ (Kazantzidis et al. 2009). However, the short relaxation time scale involved

and the lack of observational evidence of a merger with such characteristics in the last 1-2 Gyr suggest that Sgr is the most likely perturber.

It is important to note that all simulations analysed in this work considered initially stable, unperturbed stellar discs. It remains to be explored how a previously perturbed disc, either by a merger event or other dynamical process, would react to the tidal interaction with a satellite galaxy such as Sgr. Future studies should consider simulations spanning a range of masses for the Sgr progenitor, between the two limits we presented here, as well as varying Galactic disc models, which can be tuned more finely as our knowledge of the dynamics of the Milky Way expands. In addition, it remains to be studied whether perturbations from multiple satellite galaxies can be successfully disentangled.

ACKNOWLEDGMENTS

We thank the anonymous referee for the useful comments and suggestions that helped to improve this work. FAG was supported through the NSF Office of Cyberinfrastructure by grant PHY-0941373 and by the Michigan State University Institute for Cyber-Enabled Research. BWO was supported in part by the Department of Energy through the Los Alamos National Laboratory Institute for Geophysics and Planetary Physics. YSL and TCB acknowledge partial support from grants PHY 02-16783 and PHY 08-22648: Physics Frontiers Center/Joint Institute for Nuclear Astrophysics (JINA), awarded by the U.S. National Science Foundation. DA acknowledges support by the National Research Foundation of Korea to the Center for Galaxy Evolution Research. ÁV acknowledges financial support from the European Research Council under the European Communitys Seventh Framework Programme (FP7/2007-2013)/ERC grant agreement n. 202781.

Funding for SDSS-III has been provided by the Alfred P. Sloan Foundation, the Participating Institutions, the National Science Foundation, and the U.S. Department of Energy. The SDSS-III web site is <http://www.sdss3.org/>.

SDSS-III is managed by the Astrophysical Research Consortium for the Participating Institutions of the SDSS-III Collaboration, including the University of Arizona, the Brazilian Participation Group, Brookhaven National Laboratory, University of Cambridge, University of Florida, the French Participation Group, the German Participation Group, the Instituto de Astrofísica de Canarias, the Michigan State/Notre Dame/JINA Participation Group, Johns Hopkins University, Lawrence Berkeley National Laboratory, Max Planck Institute for Astrophysics, New Mexico State University, New York University, the Ohio State University, University of Portsmouth, Princeton University, University of Tokyo, the University of Utah, Vanderbilt University, University of Virginia, University of Washington, and Yale University.

REFERENCES

- Aihara H., Allende Prieto C., An D., et al., 2011, *ApJS*, 193, 29
- Antoja T.; Figueras F., Romero-Gómez M., Pichardo B., Valenzuela O., Moreno E., 2011, *MNRAS*, in press [arXiv:1106.1170]
- Antoja T., Valenzuela O., Pichardo B., Moreno E., Figueras F., Fernández D., 2009, *ApJ*, 700, L78
- Antoja T., Figueras F., Fernández D., Torra J., 2008, *A&A*, 490, 135
- Allende Prieto C., Sivarani T., Beers T. C., et al., 2008, *AJ*, 136, 2070
- An D., Johnson J. A., Beers T. C., et al., 2009a, *ApJ*, 707, L64
- An D., Pinsonneault M. H., Masseron T., et al., 2009b, *ApJ*, 700, 52
- Arifyanto M. I., Fuchs B., 2006, *A&A*, 449, 533
- Behroozi P. S., Conroy C., Wechsler R. H., 2010, *ApJ*, 717, 379
- Bensby T., Zenn A. R., Oey M. S., Feltzing S., 2007, *ApJ*, 663, 13
- Bird J. C., Kazantzidis S., Weinberg D. H., 2011, *MNRAS*, *submitted* (astro-ph/1104.0933)
- Bissantz N., Gerhard O., 2002, *MNRAS*, 330, 59
- Bullock J. S., Johnston K. V., 2005, *ApJ*, 635, 931
- Cabrera-Lavers A., Hammersley P. L., González-Fernández C., López-Corredoira M., Garzón F., Mahoney T. J., 2007, *A&A*, 465, 825
- Carollo D., Beers T. C., Chiba M. et al., 2010, *ApJ*, 712, 692
- Cole A. A., Weinberg M. D., 2002, *ApJ* 574, L43
- Conn B. C., Lewis G. F., Irwin M. J., Ibata R. A., Ferguson A. M. N., Tanvir N., Irwin J. M., 2005, *MNRAS*, 362, 475
- Conroy C., Wechsler R. H., 2009, *ApJ*, 696, 620
- Dehnen W., 2000, *AJ*, 119, 800
- Dehnen W., 1998, *AJ* 115, 238
- Dobbs C. L., Theis C., Pringle J. E., Bate M. R., 2010, *MNRAS*, 403, 625
- Elmegreen D. M., Elmegreen, B. G., 1983, *ApJ*, 267, 31
- Elmegreen D. M., Elmegreen B. G., 1982, *MNRAS*, 201, 1021
- Fux, R., 2001, *A&A*, 373, 511
- Gioachin F., Jetley P., Mendes C. L., Kale L. V., Quinn T. R., 2007, *Toward Petascale Cosmological Simulations with ChaNGa*, Tech. Rep. 07-08
- Gómez F. A., Minchev I., Villalobos A., O'Shea B. W., Williams M. E. K., 2011, *MNRAS*, 419, 216
- Gómez F. A., Helmi A., 2010, *MNRAS*, 401, 2285
- Gómez F. A., Helmi A., Brown A. G. A., Li Y. S., 2010, *MNRAS*, 408, 935
- Helmi A., de Zeeuw P. T., 2000, *MNRAS*, 319, 657
- Helmi A., White S. D. M., de Zeeuw P. T., Zhao H., 1999, *Nature*, 402, 53
- Helmi A., Navarro J. F., Meza A., Steinmetz M., Eke V. R., 2003, *ApJ*, 592, L25
- Hernquist L., 1990, *ApJ*, 356, 359
- Høg E., Fabricius C., Makarov V. V. et al., 2000, *A&A*, 355, L27
- Ibata R., Irwin M. J., Lewis G. F., Ferguson A. M. N., Tanvir N., 2003, *MNRAS*, 340, L21
- Kazantzidis S., Zentner A. R., Kravtsov A. V., Bullock J. S., Debattista V. P., 2009, *ApJ*, 700, 1896
- Kazantzidis S., Bullock J. S., Zentner A. R., Kravtsov A. V., Moustakas L. A., 2008, *ApJ*, 688, 254
- Keselman J. A., Nusser A., Peebles P. J. E., 2009, *Phys.*

- Rev. D, 80, 063517
King I. R., 1966, *AJ*, 71, 64
Klement R., Fuchs B., Rix H.-W., 2008, *ApJ*, 685, 261
Klypin A., Zhao H., Somerville R. S., 2002, *ApJ*, 573, 597
Kormendy J., Norman C. A., 1979, *ApJ*, 233, 539
Lee Y. S., et al., 2011b, *ApJ*, 738, 187
Lee Y. S., et al., 2011a, *AJ*, 141, 90.
Lee Y. S., Beers T. C., Sivarani T., et al., 2008b, *AJ*, 136, 2050
Lee Y. S., Beers T. C., Sivarani T., et al., 2008a, *AJ*, 136, 2022
Levine E. S., Blitz L., Heiles C., 2006, *Sci*, 312, 1773
Majewski S. R., Wilson J. C., Hearty F., Schiavon R. R., Skrutskie M. F., 2010, *IAU Symposium*, 265, 480
Michel-Dansac L., Abadi M. G., Navarro J. F., Steinmetz M., 2011, *MNRAS*, 414, L1
Miyamoto M., Nagai R., 1975, *PASJ*, 27, 533
Minchev I., Boily C., Siebert A., & Bienayme O., 2010, *MNRAS*, 407, 2122
Minchev I., Quillen A. C., Williams M., Freeman K. C., Nordhaus J., Siebert A., Bienayme O., 2009, *MNRAS*, 396, L56
Minchev I., Quillen A. C., 2008, *MNRAS*, 386, 157
Minchev I., Nordhaus J., Quillen A. C., 2007, *ApJ*, 664, L31
Momany Y., Zaggia S., Gilmore G., Piotto G., Carraro G., Bedin L. R., de Angeli F., 2006, *A&A*, 451, 515
Munn J., Monet D. G., Levine S. E., et al., 2004, *AJ*, 127, 3034
Munn J., Monet D. G., Levine S. E., et al., 2008, *AJ*, 136, 89
Navarro J. F., Frenk C. S., White S. D. M., 1996, *ApJ*, 462, 563
Navarro J.F., Helmi A., Freeman K. C., 2004, *ApJL*, 601, L43
Newberg H. J. et al., 2002, *ApJ*, 569, 245
Nissen P. E., Schuster, W. J., 1991, *A&A*, 251, 457
Oh S. H., Kim W.-T., Lee H. M., Kim J., 2008, *ApJ*, 683, 94
Peñarrubia J., Belokurov V., Evans N. W., Martinez Delgado D., Gilmore G., Irwin M., Niederste-Ostholt M., Zucker D. B., 2010, *MNRAS*, 408, L26
Peñarrubia J. et al., 2005, *ApJ*, 626, 128
Perryman M. A. C. et al., 2001, *A&A*, 369, 339
Perryman M. A. C. et al., 1997, *A&A*, 323, 49
Pohl M., Englmaier P., Bissantz N., 2008, *ApJ*, 677, 283
Purcell C. W., Bullock J. S., Tollerud E. J., Rocha M., Chakrabarti S., *Nature*, 477, 301
Quillen A. C., Minchev I., Bland-Hawthorn J., Haywood M., 2009, *MNRAS*, 397, 1599
Quillen A. C., Dougherty J., Bagley M. B., Minchev I., Comparella J., 2011, *MNRAS*, submitted [arXiv:1010.5745]
Quinn P. J., Hernquist L., Fullagar D. P., 1993, *ApJ*, 403, 74
Salim S., Gould A., 2003, *ApJ*, 582, 1011
Schlesinger K. J., et al., *AJ*, submitted [arXiv:1112.2214]
Schuster W. J., Moitinho A., Márquez A., Parrao L., Covarrubias E., 2006, *A&A* 445, 939
Schönrich R., Binney J., Dehnen W., 2010, *MNRAS*, 403, 1829
Smolinski J. P., Lee Y. S., Beers T. C., et al., 2011, *AJ*, 141, 89
Tutukov A. V., Fedorova A. V., 2006, *Astron. Rep.*, 50, 785
Yanny B. et al., 2003, *ApJ*, 588, 824
Yanny B. et al., 2009, *ApJ*, 137, 4377
Younger J. D., Besla G., Cox T. J., Hernquist L., Robertson B., Willman B., 2008, *ApJ*, 676, L21
Villalobos A., Helmi A., 2008, *MNRAS*, 391, 1806
Wylie-de Boer E., Freeman K., 2010, *IAU Symposium*, 262, 448